Combustion and Flame 185 (2017) 160–172

Contents lists available at ScienceDirect

Combustion and Flame

journal homepage: www.elsevier.com/locate/combustflame

Correlation effects between turbulence and the conversion rate of pulverized char particles

Jonas Krüger[a,*], Nils Erland L. Haugen[a,b], Terese Løvås[a]

[a] Department of Energy and Process Engineering, Norwegian University of Science and Technology, Kolbjørn Hejes vei 1B, Trondheim NO-7491, Norway
[b] SINTEF Energy Research, Trondheim N-7465, Norway

ARTICLE INFO

Article history:
Received 8 February 2017
Revised 4 July 2017
Accepted 10 July 2017

Keywords:
Reacting multiphase flow
Particle clustering
Heterogeneous combustion
Direct numerical simulation
Char
Turbulence

ABSTRACT

The effect of turbulence on heterogeneous reactions on the surface of char particles embedded in a turbulent oxidizer, consisting of oxygen and carbon-dioxide, is in this work studied numerically. It is shown that for a small Damköhler number (**Da**), which is the ratio between a turbulent and a chemical time scale, the char conversion rates are somewhat *increased* by the turbulence. This is found to be due to the increased mass transfer rate to the char particle surface that is caused by the turbulence-induced relative velocity between the char and the oxidizer. For large Damköhler numbers, however, the char conversion rate is strongly *reduced* due to particle clustering. This reduction is explained by the fact that when particles are clustered in densely populated particle clusters, the transfer of oxygen to the particles in the centre of the clusters is reduced since the oxygen is consumed by the particles closer to the external surface of the cluster. At the same time, high concentrations of oxygen exist in the voids between the particle clusters. This oxygen cannot take part in the conversion of the char until it is transported to the char surface. The effects of turbulence on the heterogeneous reaction rates are furthermore modelled based on Direct Numerical Simulation (DNS) data for a simplified reacting gas particle system.

1. Introduction

Numerical simulations are an important tool in predicting the performance, and planning the operation, of industrial applications involving heterogeneous reactions, such as pulverized coal combustion (PCC) or biomass gasification. To increase efficiency and decrease the environmental impact of new systems and optimize existing ones, more insight into the details of combustion processes is essential. Since combustion processes are a complex interaction of physical and chemical effects such as mass, momentum, heat and species transfer over a wide range of scales, also in conjunction with chemical reactions, detailed simulations of even just components of an industrial combustion system are challenging in respect to computational costs. This restricts simulations of industrial scale combustion systems to be very coarse and use empirical models. This is especially true if a lot of cases have to be simulated for a parametric study.

A common approach used in industry and research is the Reynolds-Averaged Navier Stokes (RANS) model [1,2]. The evolution of the particle position in turbulence can be accounted for by, among others, stochastic tracking [3], or by solving a joint PDF that is derived from probabilistic models of both the fluid and particles [4]. To account for the interaction between the turbulent flow field and chemistry, closure models for RANS have been developed that use transported PDF methods for both gas and particle phase attributes [5,6] and show good agreement with measurements of the semi-industrial IFRF furnace No.1. However, the effect of clustered particles due to turbulence on the reaction rates is not explicitly accounted for.

Recently, the first Large-Eddy simulations (LES) are employed for pilot scale systems [7–9]. The work of Stein et al. [8] presents a joint effort of three different research groups to present a comprehensive LES of pulverized coal combustion. For two of the three groups, particle dispersion is also taken into account with a stochastic component. Combustion of char is modelled using the kinetic diffusion rate model introduced by Baum and Street [10] or an intrinsic model presented by Smith [11]. For all three approaches, the obtained velocity fields show good agreement with experimental data, but there are some differences regarding the temperature and species data. The simulation of Watanabe et al. was able to predict the coal burnout along the central axis of a lab-scale coal jet flame to within measurement error, and could reproduce unstable combustion performance for a large-scale coal burner [9]. Watanabe et al. also combines LES with a flamelet model model [12] to investigate ignition and extinction of lab-scale

* Corresponding author.
E-mail address: jonas.kruger@ntnu.no (J. Krüger).

http://dx.doi.org/10.1016/j.combustflame.2017.07.008
0010-2180/

and industrial-scale burners, and coal burnout along the central burner axis is in good agreement with measurements for the lab scale burner. Ignition limits for the industrial scale burner obtained from the simulation compare well with flame images from the actual burner, and the simulation is able to successfully predict a sharp decrease in flame stability near the ignition limit.

These modelling approaches require subgrid models that account for flow and chemistry effects on scales that are smaller than what is resolved by the simulation. The subgrid models used in RANS and LES are developed by theoretical and statistical analysis of the basic processes of combustion, studying lab scale systems or numerical experiments using Direct Numerical Simulation (DNS), where all relevant turbulent scales are resolved. Although they are computationally expensive [13], DNS provide a way to non-intrusively study turbulent combustion systems and yield flow statistics that are difficult or impossible to obtain in real experiments [14]. This accurate description of the flow in DNS makes it especially suitable to study turbulent flows in detail. The insights gained can then be utilized to develop models and correlations that can be used in simulations of industrial systems.

It is known that turbulence affects combustion systems on different scales, from the recirculation zone behind a bluff body burner to the flow far downstream. Turbulence is also essential for mixing and transport of physical quantities, such as energy and species composition, which in turn have an influence on the reaction rates. For the case of homogeneous combustion, the interaction between turbulence and combustion has been studied extensively, and consequently a large variety of models have been developed. For premixed flames e.g., models that are based on the interaction of scales [15], probabilities to find either burned or unburned gases [16,17], or geometrical descriptions of the flame [18,19] can be used. In the case of non premixed flames with infinitely fast chemistry, one can use a presumed Probability Density Function (PDF) [20] or the Eddy Dissipation Concept (EDM), where the reactions are limited by either a deficiency of fuel, oxidizer or energy [21], or the Conditional Moment Closure (CMC), where all variable parameters are conditionally averaged on flow parameters such as the mixture fraction [22,23]. If the chemistry is not assumed to be infinitely fast, the reaction rates may be obtained from flamelet libraries based on presumed PDFs of unsteady flamelets to account for transient effects [24] or local chemical equilibrium if the chemical time is still much smaller than the convective or diffusive time scales [25]. Each of these models have individual strengths and shortcomings making them applicable to different combustion conditions. The review paper by Veynante and Vervisch [26] and the book by Poinsot and Veynante [27] provide an excellent overview over the state of homogeneous combustion research and the models for turbulence chemistry interaction in use and development.

Combustion of solid matter adds more complexity to the phenomena of turbulence chemistry interaction due to the multi phase nature of the problem. Depending on the composition of the fuel, each particle has to undergo drying, devolatilization/pyrolysis and finally heterogeneous combustion, all of which have to be accounted for in a complete description of the combustion process [28]. Compared to the heating and devolatilization processes, and even the conversion of devolatilized fuels, the combustion of fuel through heterogeneous reactions is slow [29,30], which makes an accurate prediction of the process all the more crucial for achieving good combustion efficiency. The interested reader is referred to the article of Eaton et al. [31] for a review on models used in pulverized coal combustion. However, to the authors' knowledge, there is no turbulence-chemistry model connecting the effect of turbulence to the process of conversion of a dried, devolatilized char particle, which is the objective of the present work.

A reacting particle and the surrounding turbulent flow are interacting on different scales, and these effects can increase or decrease the reaction rate depending on turbulence intensity. At the scale of a particle, the flow around the particle is responsible for transporting reaction products away from the particle surface, and bringing reactants to it. Additionally, turbulence increases heat transfer from and to the particle, leading to a change in the speed of reaction [32]. On larger scales, turbulence leads to a preferential concentration of particles [33,34], where particles form dense particle clusters, separated by voids where nearly no particles are present. This can separate the solid fuel from the gaseous oxidizer. Describing the shape and size of these particle clusters and voids is a major research field in itself [35].

Annamalai and Ramalingam [36] performed a theoretical study of the combustion behaviour of clusters of coal particles in a quiescent flow and identify three distinct regimes, which are defined by low, medium or high particle concentrations inside the clusters. The Individual Particle Combustion (IPC) regime is characterized by that the distances between particles are so high that their interaction can be neglected. For medium particle concentrations, the particles on the outside of the clusters consume the oxidizer fast enough so that particles on the inside of the cluster react under fuel-richer conditions, which is called Group Combustion (GC). Finally, for high particle concentrations, the outermost shell of particles consumes all the oxidizer which is transported to it, effectively preventing oxidizing species transport to the internal particles. This combustion regime is called Sheath Combustion (SC), as only the sheath of the particle cluster is reacting. These regimes were found to have different combustion rates [36]. It is reported that in the IPC, a decrease in particle size (by particle break up, leading to a increase in particle number) results in an increase in the surface specific burning rate. In the SC regime, a decrease in particle size may result in a decrease of the surface specific burning rate. A similar finding is reported by Reveillon and Demoulin [37], who examined the evaporation behaviour of droplets in turbulent flows and found that the evaporation rate inside droplet clusters is slower than on the outside. This is due to the fast saturation of the fluid inside the droplet clusters and the slow mixing of saturated and unsaturated fluid.

Due to the increase of available computing power, DNS of pulverized coal jets under highly turbulent conditions have recently been published, providing insights into this complex phenomenon. Luo et al. performed a DNS of a pulverized coal jet flame [29] for a Reynolds number of around 30000 and compare their results qualitatively with experiments. They identify GC regimes at the jet nozzle and IPC regimes further downstream in the jet. The same numerical approach has been used to investigate the flame structures in a pulverized coal jet flame [38]. It is found that pulverized coal flames feature both premixed and non-premixed combustion, with non-premixed combustion dominating. A lab-scale pulverized coal jet flame was studied by Hara et al. [39], who propose a simple global reaction scheme that takes into account the effects of devolatilization products on the homogeneous reactions. A good agreement on the particle motion between simulation and experiments is reported. Moreover, they find different combustion regimes in the inner and outer flame layer. Brosh and Chakraborty investigated the effect of equivalence ratios and velocity fluctuations on pulverized coal combustion [40] and ignition [41] and found that the premixed combustion regime (which is more similar to IPC and GC than to SC) is more prominent for higher turbulent velocity fluctuations and vice versa. Moreover, an increase in velocity fluctuations is beneficial for mixing, but too high velocity fluctuations lead to flame extinction by increasing the heat transfer from the flame kernel. However, the published studies focus either on early stages of the combustion, where devolatilized fuel is the main driver of combustion [40], or on flows

with non-isotropic turbulence [39]. Muto et al. studied coal particle swelling due to devolatilization and its effect on combustion in a pulverized coal jet flame [42]. The simulation code and the simulated flame are the same as in the study of Hara et al. [39]. For this setup, taking into account particle swelling and shrinkage had no significant effect on the gas temperature distribution. While all studies account for char conversion, it is not explicitly studied.

The present work is part of an effort to provide a subgrid model to account for the effect of turbulence on heterogeneous reactions (such as char oxidation). DNS is used to study clustered char particles in a turbulent reacting flow and analyse the effect of changing Damköhler numbers on the char oxidation rates. The Damköhler number relates the typical time scale of mixing to the time scale of a chemical reaction. Here, the turbulent integral time scale is taken as the mixing time scale, and the time scale of a diffusion limited chemical reaction (described in Section 3) describes the chemical time scale. This is an extension of earlier work that studied this effect in a simplified setup [43,44], where the isothermal consumption of a passive scalar by particles in a turbulent flow was studied by DNS. This work is now extended to a DNS with heterogeneous reactions between reactive chemical species in order to study the interaction between the kinetics of heterogeneous reactions and turbulent clustering.

Although complex char oxidation reaction mechanisms exist [45,46], the wide range of time scales of the individual reactions make a deduction of basic flow properties and timescales used in the analysis complicated. Moreover, calculating and storing many species and their reaction rates for both flow field and a large number of particles is prohibitively expensive, hence a simple mechanism is used in this work, although the mathematical framework is developed for a generic kinetic case. This also reduces the complexity and significantly simplifies the analysis of the data obtained from the simulations.

The combustion process investigated in this work is represented by oxy-fuel combustion, which has been proposed as one measure to implement carbon capture technologies, and hence, decrease the environmental impact of fossil fuelled energy generation, as summarized in the review paper of Chen et al. [47]. The main difference between oxy-fuel and conventional combustion is that instead of air, pure oxygen together with recirculated flue gases, mainly CO_2, is used as oxidizing agent. Thus, it represents a simple case to study when only oxygen is assumed to be the oxidizing species. This further reduces the computational effort compared to an air fired case, as the absence of nitrogen yields a lower number of species as well as true binary diffusion.

The paper first gives an overview of the equations that are used to describe the fluid, the particles and their interaction in Section 2, followed by an introduction of all dimensionless numbers in Section 3. Thereafter, a model is proposed to describe the effect of turbulent clustering on the heterogeneous reaction rates, followed by the boundary and initial conditions of the DNS cases in Section 5. In Section 6, the data obtained is shown and compared with the proposed model, followed by a short discussion of the results and future work in Section 7.

2. Numerical modelling

2.1. Fluid equations

For the DNS simulations shown in this work, “The Pencil-Code” [48] is used, which is a an open source CFD code. It solves the fluid equations using a sixth-order finite difference scheme for spatial discretization and a compact third-order Runge–Kutta scheme [49] for temporal discretization. Gravity is neglected for both particle and fluid phase for simplicity and all domain boundaries are periodic. The implementation of the homogeneous chemistry has previously been described in detail by Babkovskaia et al. [50]. The continuity equation is solved as

$$\frac{\mathrm{D}\rho}{\mathrm{D}t} = -\rho\nabla\cdot\boldsymbol{u} + S_\rho, \tag{1}$$

where $\mathrm{D}/\mathrm{D}t = \partial/\partial t + \boldsymbol{u}\cdot\nabla$ is the advective derivative, ρ is the density, $\boldsymbol{u}$ is the velocity and S_ρ is the mass source term due to mass transfer from the particles to the fluid. All source terms present in the fluid equations are explained in Section 2.2. The momentum equation is written in the form

$$\rho\frac{\mathrm{D}\boldsymbol{u}}{\mathrm{D}t} = -\nabla p + \nabla\cdot\tau + \boldsymbol{f} + S_{m,p}, \tag{2}$$

where p is pressure and $\boldsymbol{f}$ is a volume force, which in the present work is given by a turbulent forcing. The forcing at time t and position x is given by

$$\boldsymbol{f}(x,t) = Real\big(N\boldsymbol{f}_{w(t)}\exp[iw(t)\cdot x + i\phi(t)]\big), \tag{3}$$

where the wave vector $w(t)$ and the random phase $\phi(t)$ are changing at every time step, and N is a normalization factor. The forcing employs nonhelical transversal waves of the form

$$\boldsymbol{f}_w = \frac{(w\times e)}{\sqrt{w^2-(w\cdot e)^2}}, \tag{4}$$

where e is a unit vector not aligned with w. This approach yields forcing that is correlated in space, but not in time. It essentially introduces shear at large scales, which is found in real applications. The forcing mechanism, which has been used in many studies, is described in detail in the work of Brandenburg et al. [51] and yields homogeneous isotropic turbulence. The viscous stress is given by:

$$\tau = 2\rho\boldsymbol{\mu}\boldsymbol{S}, \tag{5}$$

where $\boldsymbol{S} = (1/2)(\partial u_i/\partial x_j + \partial u_j/\partial x_i) - (1/3)\delta_{ij}\nabla\cdot\boldsymbol{u}$ is the traceless rate of strain tensor. Since the resolution in all cases is sufficient to resolve the smallest scales of the turbulence, no modelling of turbulence is required. The term $S_{m,p}$ in Eq. (2) accounts for the momentum that is transferred to the fluid by the mass that is released from the particle. The equation for the mass fraction of each species is given by

$$\rho\frac{\mathrm{D}Y_k}{\mathrm{D}t} = -\nabla\cdot\boldsymbol{J}_k + \dot{\omega}_k + S_{y,k}, \tag{6}$$

where Y_k is the mass fraction of species k, $\boldsymbol{J}_k$ is the diffusive flux and $\dot{\omega}_k$ is the chemical source term of species k due to homogeneous reactions, described in detail in the work of Babkovskaia et al. [50], and $S_{y,k}$ is the source term due to gas phase species being involved in heterogeneous reactions. The diffusive flux of species k is given by

$$\boldsymbol{J}_k = \rho Y_k\boldsymbol{V}_k \tag{7}$$

when $\boldsymbol{V}_k$ is the diffusive velocity of species k. Finally, the energy equation [50] is

$$c_v\frac{\mathrm{D}\ln T_g}{\mathrm{D}t} = \sum_k^{N_{species}}\left(-\nabla\cdot\boldsymbol{J} + \dot{\omega}_k\right)\left(\frac{R}{m_k} - \frac{h_{s,k}}{T_g}\right) - \frac{R}{m_k}\nabla\cdot\boldsymbol{u} + \frac{2\boldsymbol{\mu}\boldsymbol{S}^2}{T_g} - \frac{\nabla\cdot\mathbf{q}}{\rho T_g} + S_{T,conv} + S_{enth}, \tag{8}$$

where T_g is the gas temperature, c_v is the heat capacity at constant volume, R is the universal gas constant, $h_{s,k}$ is the sensible enthalpy of species k, m_k is the molar mass of species k,

$$\boldsymbol{q} = \sum_k^{N_{species}} h_k\boldsymbol{J}_k - k_g\nabla T_g \tag{9}$$

is the heat flux and $h_k = h_{s,k} + \Delta h^0_{f,k}$ becomes the enthalpy of species k when $\Delta h^0_{f,k}$ is the heat of formation of species k. The thermal conductivity is given by k_g. In the above equation, the sum of the conductive and convective heat transfer from the particles to the gas is given by $S_{T,\,conv}$. The mass that is transferred to the fluid carries enthalpy with it, which is accounted for by the term S_{enth}.

2.2. Particle source terms

The mass source term due to particle mass loss in Eq. (1) is given by:

$$S_\rho = \frac{-1}{\delta V}\sum_i^{N_{p,cell}} \frac{dm_{p,i}}{dt}. \tag{10}$$

In the above equation, $m_{p,i}$ represents the mass of particle number i and δV is an arbitrary control volume to which the transfer term is applied, which in the present work is the volume of one grid cell. Since there can be more than one particle in one cell a summation over all particles i in a grid cell is required. The number of particles in the cell is given by $N_{p,cell}$.

The momentum transfer due to mass transfer from particle to fluid in Eq. (2) is given by

$$S_{m,p} = \frac{1}{\delta V}\sum_i \dot{m}_{p,i}(\boldsymbol{u} - \boldsymbol{v}_{p,i}), \tag{11}$$

where $\boldsymbol{v}_{p,i}$ is the velocity of particle i. The species source term coming from particle reactions in Eq. (6) is given by

$$S_{y,k} = \frac{1}{\delta V}\sum_i^{N_{p,cell}} \left(\dot{W}_{k,i} + Y_k \frac{dm_{p,i}}{dt}\right). \tag{12}$$

Here, $\dot{W}_{k,i}$ is the source of gas phase species k due to heterogeneous reactions on particle i (see Eq. (29)).

The energy source term due to convective and conductive heat transfer from particle to fluid in Eq. (8) is

$$S_{T,conv} = \frac{1}{\delta V}\frac{1}{\rho T_g}\sum_i^{N_{p,cell}} Q_{c,i}, \tag{13}$$

when

$$Q_{c,i} = H_i A_{p,i}(T_{p,i} - T_g), \tag{14}$$

is the heat transfer from particle to fluid and the temperature of particle i is $T_{p,i}$ and its surface area is $A_{p,i} = 4\pi r_{p,i}$, where $r_{p,i}$ is the particle radius.

The energy that is carried by the mass transfer from particle to fluid in Eq. (8) is calculated by

$$S_{enth} = \frac{1}{\delta V}\frac{1}{\rho T_g}\sum_i^{N_{p,cell}} \dot{W}_{k,i} h_{k,i}(T_{phase}). \tag{15}$$

The temperature T_{phase}, at which the species enthalpy is evaluated is taken from the phase where the species originated. When gas phase species are consumed, the enthalpy is evaluated at the gas phase temperature, if the species in question is produced by the particle, its enthalpy is evaluated at the particle temperature. The heat transfer coefficient H_i, taken from [52], can be expressed as

$$H_i = \frac{\mathrm{Nu}_i k_g}{2r_{p,i}}\frac{B_i}{\exp(B_i) - 1} \tag{16}$$

when Nu_i is the Nusselt number obtained from the Ranz–Marshall [32] correlation:

$$\mathrm{Nu}_i = 2 + 0.6\mathrm{Re}_{p,i}^{0.5}\mathrm{Pr}^{0.33} \tag{17}$$

with Pr being the Prandtl number of the fluid, calculated as

$$\mathrm{Pr} = \frac{\mu c_p}{k_g}, \tag{18}$$

where μ is the dynamic viscosity of the fluid and c_p the heat capacity at constant pressure. The particle Reynolds number is given by

$$\mathrm{Re}_{p,i} = \frac{d_{p,i}|\boldsymbol{v}_{p,i} - \boldsymbol{u}|}{\nu}, \tag{19}$$

when $d_{p,i} = 2r_{p,i}$ is the particle diameter. The Stefan flow constant in Eq. (16) is given by

$$B_i = \frac{\dot{m}_{p,i} c_\nu}{2\pi r_{p,i}\mathrm{Nu}_i k_g}. \tag{20}$$

In this work, we use the ideal gas equation of state, such that the pressure is found as

$$p = \frac{\rho R T}{m}. \tag{21}$$

Detailed expressions for viscosity, species diffusion, thermal conduction, enthalpy and heat capacity are found in [50].

To increase the numerical stability of the simulations, the particle related source terms in the fluid equations S_ρ, $S_{Y,k}$, $S_{m,p}$, and S_{enth} are stored in temporary scalar or vector fields and diffused by Laplacian diffusion before being added to the fluid cells. A general flow variable θ_0 is stored in a scalar field, using a projection onto neighbouring nodes (PNN) method before the diffusion steps are performed. The value of the variable is then, after the nth diffusion step:

$$\theta_{n+1} = \theta_n + \frac{D_{num}\Delta t}{N_{step}}\nabla^2\theta_n, \tag{22}$$

when D_{num} is a numerical diffusion coefficient, Δt is the simulation timestep and N_{step} is the total number of diffusion steps that are performed on the scalar field before it is applied to the respective grid nodes. This is done once per global timestep. A compact 6th order scheme is used to obtain the second derivative. The diffusion coefficient D_{num} is chosen as small as possible while still ensuring stability for the simulations. With this set-up, 80% of the total mass, energy or species transfer from the particle to the fluid is added to nodes directly neighbouring the node the particle is closest to. The effect of diffusing the scalar field is comparable with spatial filtering with a Gaussian filter with a standard deviation of $0.3\Delta x$. This approach greatly stabilizes the simulations without significantly changing the dynamics of the flow. An alternative to the approach described above is to use a spatial filter to distribute the effect of a particle onto several fluid grid points. The spatial filter would typically be a weighted distribution over the fluid grid points in the neighbourhood of the particle. For more numerical stability, a spatial filter with a larger radius of influence will be needed, which means that the effect of the particle will be distributed over more grid points. The effect of the radius of influence in such methods is studied by Sundaram and Collins [53]. During the development of the method used in the current work, comparisons with established interpolation methods for particle-fluid transfers, like the particle-in-cell-method (PIC) of Squires and Eaton [54] and the (PNN) method as used by Elghobashi and Truesdell [55], have been performed. The comparisons were performed for particle number densities where both PIC and PNN were stable. Timeseries of key simulation attributes, such as particle and gas temperature and particle mass loss, were between the results that PNN and PIC yielded.

2.3. The particle equations

The particle model of the Pencil-Code has been extended to account for reactive particles, which exchange momentum, mass,

species and energy with the fluid. A detailed description of the particle reaction model can be found in Haugen et al. [52,56]. The only momentum transfer from the particles to the fluid is via the mass they transfer to the fluid. The back reaction due to the particle drag force is not considered in this work, since its focus does not lie on turbulence statistics. The particles are regarded as point particles, displacing no fluid, which is valid for particles that are much smaller than the grid cells. Furthermore, particle-particle interactions are not considered due to the dilute nature of the flow. Particle tracking is achieved using a Lagrangian formalism where the evolution equation for the particle velocity is given as

$$\frac{\mathrm{d}\boldsymbol{v}_p}{\mathrm{d}t} = \frac{\boldsymbol{F}_p}{m_p}, \tag{23}$$

and for the position as

$$\frac{\mathrm{d}\boldsymbol{x}}{\mathrm{d}t} = \boldsymbol{v}_p, \tag{24}$$

where m_p, $\boldsymbol{v}_p$ and $\boldsymbol{x}$ are the mass, velocity and position of the particle's centre of mass, respectively. Furthermore, the force $\boldsymbol{F}_p$ is the sum of all forces acting on the particle. Since gravity is neglected, and since a high density ratio between the particles and the fluid is assumed, the only force on the particles that has to be considered is the drag force. The Stokes drag, with extension to low and medium particle Reynolds numbers, is used in the present work. This means that the total force acting on the particles is given by

$$\boldsymbol{F}_p = \frac{1}{2}\rho C_D A_p |\boldsymbol{u} - \boldsymbol{v}_p|(\boldsymbol{u} - \boldsymbol{v}_p) = \frac{m_p}{\tau_p}(\boldsymbol{u} - \boldsymbol{v}_p), \tag{25}$$

when

$$\tau_p = \frac{2m_p}{\rho C_D \pi r_p^2 |\boldsymbol{u} - \boldsymbol{v}_p|} = \frac{8\rho_p r_p}{3\rho C_D |\boldsymbol{u} - \boldsymbol{v}_p|} = \frac{S d_p^2}{18\nu(1 + f_c)} \tag{26}$$

is the particle response time (Stokes time). In this equation, $S = \rho_p/\rho$ is the density ratio between a particle and the fluid. The extended Stokes drag coefficient is

$$C_D = \frac{24}{\mathrm{Re}_p}(1 + f_c), \tag{27}$$

where $f_c = 0.15\mathrm{Re}_p^{0.687}$ is due to the Schiller–Naumann correlation, which is valid for particle Reynolds numbers up to 800 [57]. The particles in our simulations have a mean particle Reynolds number of 0.1. The mass loss rate of a single particle is calculated as:

$$\frac{dm_p}{dt} = -\sum_{k}^{N_{species}} \dot{W}_k, \tag{28}$$

while the net species mass production rate is given by

$$\dot{W}_k = A_p \widehat{RR}_k M_k. \tag{29}$$

The surface area of the particle is denoted A_p, the molar mass of species k is M_k and

$$\widehat{RR}_k = \sum_{j}^{N_{reactions,het}} (\nu''_{j,k} - \nu'_{j,k})\widehat{R}_j \tag{30}$$

is the surface specific molar production rate of species k. The stoichiometric coefficients $\nu'_{j,k}$ and $\nu''_{j,k}$ are for the reactant and product side of reaction j, respectively. The rate of reaction j is given by:

$$\widehat{R}_j = k_{kin,j}\left(\prod_{l}^{N_{species}} \left(X_{l,s}C_g\right)^{\nu'_{j,l}}\right). \tag{31}$$

Here, $X_{l,s}$ is the mole-fraction of species l at the particle surface, C_g is the local gas concentration, which is evaluated at the particle film temperature $T_{film} = T_p + (T_g - T_p)/3$ and found from the ideal gas law;

$$C_g = \frac{N_m}{V} = \frac{p}{RT_{film}}. \tag{32}$$

In this equation, N_m represents the number of moles in the volume V. The kinetic rate of reaction j is given by the Arrhenius expression

$$k_{kin,j} = B_{n,j}T^{\alpha_{n,j}}\exp(-E_{an,j}/RT_p), \tag{33}$$

where B_n is the pre-exponential factor, α_n is the temperature exponent, and E_{an} the activation energy, which are all empirical coefficients that are given by the kinetic mechanism.

For a single irreversible global heterogeneous reaction with only one homogeneous reactant species r, an algebraic solution for the surface mole fraction $X_{r,s}$ of the reactant can be found by applying the Baum and Street model [10] and assuming equilibrium between the transport and consumption of the reactant r:

$$\underbrace{X_{r,s}\dot{n}_{\mathrm{total}}}_{Stefan\ Flow} - \underbrace{C_g k_{diff}(X_{r,\infty} - X_{r,s})}_{Diffusion} = \underbrace{C_g k_{kin} X_{r,s}}_{Production/Consumption}. \tag{34}$$

If the heterogeneous reaction is unimolar, i.e. $\dot{n}_{total} = 0$, Eq. (34) gives a very simple expression for the mole fraction of reactant r at the particle surface;

$$X_{r,s} = \frac{X_{r,\infty}k_{diff}}{k_{kin} + k_{diff}}, \tag{35}$$

when k_{diff} is the mass transfer coefficient. For multiple reactant species, a multivariate set of Eq. (35) can be solved by a Newton–Raphson method. The expression in Eq. (35) makes it possible to use the mean reactant mole fraction in the grid cell, $X_{r,\infty}$, instead of the reactant mole fraction at the particle surface, $X_{r,s}$. This approach can only be used when the volume of the boundary layer around the particle is much smaller than the volume of the grid cell, which necessitates small particles. For a single reaction with one reactant species, Eq. (31) then reduces to

$$\widehat{R} = k_{eff}X_{r,\infty}C_g, \tag{36}$$

when the mean effective reaction coefficient,

$$k_{eff} = \frac{k_{kin}k_{diff}}{k_{kin} + k_{diff}}, \tag{37}$$

is introduced to account for kinetic reaction rate as well as diffusive transport of reactant to the particle. The term k_{diff} is the mass transfer rate, which is defined by

$$k_{diff} = \frac{D\mathrm{Sh}}{2r_p}, \tag{38}$$

where D is the diffusivity in the bulk gas and

$$\mathrm{Sh} = 2 + 0.69\mathrm{Re}_p^{0.5}\mathrm{Sc}^{0.33} \tag{39}$$

is the particle Sherwood number, which is obtained using the Ranz–Marshall correlation [32] for flows with low and intermediate Reynolds numbers. Here, Re_p is the particle Reynolds number and Sc the Schmidt number. It is interesting to note that for a RANS simulation, the relative velocity between the particles and the fluid cannot be resolved and has to be modelled. In many RANS modelling tools, it is therefore customary to include some kind of particle dispersion model, where the particles are displaced in random directions and distances based on the local turbulence parameters in order to make the particles diffuse through the fluid. As a by-product of the particle dispersion that is obtained with these models, there will be a relative velocity between the particles and the fluid, but, since no account is made for the correlation with the instantaneous turbulent structures, this velocity does not have

anything to do with the reality. It is therefore often better to simply neglect the effect of the relative particle-fluid velocity by setting the particle Reynolds number in Eq. (39) to zero, such that the Sherwood number becomes 2. Hence, for a quiescent fluid, or for a RANS simulation, the Sherwood number is 2 and the mass transfer coefficient then reduces to

$$k_{diff,q} = D/r_p. \tag{40}$$

The particle temperature evolution is given by:

$$\frac{dT_p}{dt} = \frac{1}{m_p c_{p,p}}(Q_{reac} - Q_c + Q_{rad}), \tag{41}$$

where Q_{reac} is the heat due to the surface reactions, Q_c the conductive heat loss to the fluid and $Q_{rad} = 4\epsilon\sigma\pi r_p^2(T_s^4 - T_p^4)$ is the radiative heating of the particle. Here, ϵ is the emissivity, σ the Stefan–Boltzmann constant and T_s is the temperature of the surroundings. If $T_p > T_s$, this corresponds to a situation where the particles are radiatively cooled, acting as heat sinks in the system. The particle heat capacity is denoted by $c_{p,p}$. The particle is assumed to be thermally thin, resulting in a uniform temperature distribution throughout the particle.

The reactive heating rate is given by:

$$Q_{reac} = A_{p,i} \sum_{j}^{n_{reactions}} \widehat{R}_j h_j, \tag{42}$$

when the heating due to reaction j is composed of the surface specific reaction rate $\widehat{R}_j$ and the heat of reaction h_j. The specific enthalpies are calculated at the particle temperature for all products and for all solid reactants, and at the gas temperature for gaseous reactants. The reactive heating only heats up the particle, as the heat loss to the fluid is already accounted for by evaluating the species enthalpy that is transferred to the fluid at the particles temperature in the term S_{enth} in Eq. (15).

3. Dimensionless numbers

In this work, four dimensionless numbers are of special interest and therefore explained in detail: The Damköhler number Da, the Sherwood number Sh, which is introduced in Eq. (39), the particle Stokes number St and the Sherwood correction factor $\tilde{\alpha}$. The Damköhler number is the ratio between the turbulent time scale τ_L and the chemical time scale τ_{hom}:

$$\mathrm{Da} = \frac{\tau_L}{\tau_{hom}}, \tag{43}$$

where τ_{hom} is the inverse of the ideal homogeneous reaction rate. If we assume a reactive object, which is typically a particle or a dense cluster of particles, the ideal homogeneous reaction rate then depends on the mean reactive surface area of the object $\overline{A}'$, the mean reactive density $\overline{n}'$ and its effective reaction rate $\overline{k}'_{eff}$. Accordingly, τ_{hom} can be expressed as

$$\tau_{hom} = \frac{1}{\alpha_{hom}} = \frac{1}{\overline{A}'\overline{n}'\overline{k}'_{eff}}, \tag{44}$$

such that the Damköhler number becomes:

$$\mathrm{Da} = \alpha_{hom}\tau_L = \overline{A}'\overline{n}'\overline{k}'_{eff}\tau_L. \tag{45}$$

The turbulent time scale considered in this work is the time scale τ_L of the integral scale, $L = L_{dom}k_{dom}/k_f$, where k_{dom} is the wavenumber of the domain size L_{dom} and k_f is the wave number of the external forcing. Subsequently τ_L is given by

$$\tau_L = \frac{L_{dom}k_{dom}}{k_f u_{\mathrm{RMS}}}, \tag{46}$$

where the root mean square velocity is u_{RMS}. The particle Stokes number is given by the ratio between the particle response time and the turbulent time scale:

$$\mathrm{St} = \frac{\tau_p}{\tau_L}. \tag{47}$$

To achieve clustering at the large scales of the flow, the density and radius of the particles are chosen so that for the simulations in this work a Stokes number of approximately 1 is achieved. For low Da, the fluid composition and temperature is relatively homogeneously distributed throughout the domain. This means that the fluid surrounding a given particle is not directly influenced by the particles in its immediate neighbourhood, but rather by the accumulated effect of all particles in the domain. Thus, the reaction rate, and hence also the Damköhler number, scale proportionally to the mean surface area of the particles $\overline{A}' = \overline{A}_p$, the mean particle number density in the domain $\overline{n}' = \overline{n}_p$ and mean effective particle reaction rate $\overline{k}'_{eff} = \overline{k}_{eff,p}$, which means that the Damköhler is given by

$$\mathrm{Da} = \overline{A}_p\overline{n}_p\overline{k}_{eff,p}\tau_L = \alpha_{hom,q}\tau_L, \tag{48}$$

when the ideal homogeneous reaction rate is

$$\alpha_{hom,q} = \overline{A}_p\overline{n}_p\overline{k}_{eff,p}, \tag{49}$$

for a quiescent fluid (Sh=2) and a mean effective particle reaction rate $\overline{k}_{eff,p}$ that is equal to the mass transfer rate k_{diff}, is established as a base value to compare against. This case, when $k_{diff} = k_{eff,p}$, corresponds to the situation when $k_{diff} \ll k_{kin}$, i.e., when the reactions are diffusion controlled. The ideal homogeneous reaction rate is also used to define the Damköhler number of each case.

4. Heterogeneous combustion regimes

4.1. Low Damköhler number, IPC regime

For low **Da** and diffusion limited reaction rates, the actual reaction rate is higher than the ideal homogeneous reaction rate. This is due to the fact that the ideal homogeneous reaction rate (Eq. (49)) is based on a quiescent flow, for which the Sherwood number is 2 according to the Ranz-Marshall correlation [32]. The actual Sherwood number is higher than 2 because of the relative motion of particle and fluid. The increase in the reaction rate becomes the ratio of the actual Sherwood number divided by two. When account is made for the relative fluid-particle velocity due to turbulence, the mean effective diffusion limited particle reaction rate is therefore given by:

$$\underbrace{\alpha_{hom,t}}_{turbulent} = \alpha_{hom,q}\frac{\mathrm{Sh}}{2}. \tag{50}$$

Note that in this regime, the reaction rate still scales linearly with the number density of particles, $\overline{n}_p$. Since each particle is reacting without influencing other particles, its combustion regime is comparable to Individual Particle Combustion [36].

4.2. High Damköhler number, SC regime

It is known that particles embedded in a turbulent flow will form particle clusters where the particle number density is significantly above the mean value [33–35]. For large Da, the particle number density inside these clusters is very high and the internal oxygen is consumed rapidly. Following the description in the work of Haugen et al. [44], the characteristic length scale l of these particle clusters is obtained by assuming that the eddies responsible for the clustering have the same time scale as the clustering particles, such that $\tau_l = \tau_p = \mathrm{St}\tau_L$. Assuming Kolmogorov scaling between the scales l and L, one obtains $l = L\mathrm{St}^{3/2}$ and $D_{diff,cl} = u_l l =$

$u_{\mathrm{RMS}} L \mathrm{St}^2$ [44]. The subscript *cl* stands for all cluster related properties. After the internal oxygen is consumed, the reaction rate is limited by the transport of oxygen to the surface of the particle clusters. This is a combustion regime similar to Sheath Combustion [36], and the reaction rate converges to a *particle number density independent* value α_{cl} [44]:

$$\alpha_{cl} = \overline{A}_{cl}\overline{n}_{cl}\overline{k}_{diff,cl} = A_1 A_2 \frac{D_{diff,cl}\overline{\mathrm{Sh}}}{l^2}. \tag{51}$$

The cluster dependent reaction rate, α_{cl}, is dependent on the mean cluster surface area $\overline{A}_{cl} = A_1 l^2$, the mean cluster number density $\overline{n}_{cl} = A_2/l^3$ and the cluster dependent mass transfer rate $\overline{k}_{diff,cl} = D_{diff,cl}\mathrm{Sh}/l$, where A_1 and A_2 are fitting factors related to the shape of the particle clusters, influencing their number and surface area, respectively. Inserting the expressions for l and $D_{diff,cl}$ into Eq. (51) then yields:

$$\alpha_{cl} = \frac{A_1 A_2 \overline{\mathrm{Sh}}}{\tau_L \mathrm{St}}. \tag{52}$$

Haugen et al. [44] determined values for A_1A_2 for a range of Re_L and St and they arrive at the following functional dependence; $A_1A_2 = 0.08 + \mathrm{St}/3$, which predicts the effect of turbulent clustering on the reaction rate in a simpler system. Note that the expression for α_{cl} has no dependence on the number of individual particles.

4.3. Connecting IPC and SC combustion regimes

A model for the reaction rate connecting the limits for small and large **Da** (IPC and SC in Annamalai and Ramalingam) can be obtained by constructing the harmonic mean:

$$\alpha = \frac{\alpha_{cl}\alpha_{hom,t}}{\alpha_{cl} + \alpha_{hom,t}}. \tag{53}$$

By dividing this expression by the ideal homogeneous reaction rate for a quiescent fluid, a Sherwood correction factor $\tilde{\alpha} = \alpha/\alpha_{hom,q}$ can be found as:

$$\tilde{\alpha} = \frac{\alpha_{cl}}{\alpha_{cl} + \mathrm{DaSh}/(2\tau_L)} \frac{\overline{\mathrm{Sh}}}{2}. \tag{54}$$

This expression takes into account both the influence of the turbulence on each individual particle via the Sherwood number, as well as the influence of large scale clustering via the cluster dependent reaction rate α_{cl}.

If the chemical timescale, the turbulent flow time scale and the particle Stokes number are known properties, the Sherwood correction factor can be combined with Eq. (40) to obtain a mass transfer rate

$$k_{diff,turb} = \tilde{\alpha} k_{diff,q} \tag{55}$$

that takes into account the effect of small scale turbulence and turbulent clustering.

4.4. Finding the Sherwood correction factor from simulations

To validate the model in Eq. (54), we compare the mean mass loss rates of the particles obtained from the DNS simulations with the mean homogeneous mass loss rate of the same case. If none of the models described in Section 1 is used in RANS simulations, a mass loss rate assuming homogeneously distributed particles reacting in a quiescent, perfectly mixed fluid is obtained for each individual computational cell. The aim of this paper is to provide a model for heterogeneous combustion of char that accounts for the effects of turbulence and that is easily implemented into commercial RANS CFD software.

Based on Eq. (37), the mean effective reaction coefficient in a quiescent fluid is given by

$$k_{eff,q} = \frac{k_{kin}k_{diff,q}}{k_{kin} + k_{diff,q}}, \tag{56}$$

when $k_{diff,q}$ is found from Eq. (40). The mean homogeneous mass loss rate is found by combining Eqs. (28) and (29), such that

$$\frac{d\overline{m}_{p,hom}}{dt} = -\overline{A}_p M_k \sum_k^{N_{species}} \widehat{RR}_k. \tag{57}$$

For a single reaction with only one reactant, where the reaction removes one carbon atom from the surface of the char particle, Eqs. (56) and (57) can then be combined with Eqs. (30) and (36) to yield

$$\frac{d\overline{m}_{p,hom}}{dt} = -\overline{A}_p M_c \overline{k}_{eff,q} \overline{X}_{r,\infty} \overline{C}_g. \tag{58}$$

As argued in Section 4.3, the turbulence only affects the mass transfer rate to the particles, not the kinetic rate. The corresponding mean effective reaction coefficient that incorporates the effect of turbulence is therefore given by

$$k_{eff,turb} = \frac{k_{kin}k_{diff,turb}}{k_{kin} + k_{diff,turb}}, \tag{59}$$

when $k_{diff,turb}$ is found from Eq. (55). Hence, the actual mass loss rate in a turbulent flow is given by

$$\frac{d\overline{m}_p}{dt} = -\overline{A}_p M_c \overline{k}_{eff,turb} \overline{X}_{r,\infty} \overline{C}_g. \tag{60}$$

By combining Eqs. (58) and (60), the ratio of the mean *actual* mass loss rate, which includes the effect of turbulence, to the mean homogeneous mass loss rate, which neglects the effect of turbulence, is found to be

$$\beta = \frac{d\overline{m}_p/dt}{d\overline{m}_{p,hom}/dt} = \frac{k_{eff,turb}}{k_{eff,hom}}. \tag{61}$$

This is a measure of how fast the reactions proceed compared to the homogeneous assumption. From Eqs. (56) and (59), it can then shown that

$$\beta = \frac{k_{kin}\tilde{\alpha}k_{diff,q}/(k_{kin} + \tilde{\alpha}k_{diff,q})}{k_{kin}k_{diff,q}/(k_{kin} + k_{diff,q})} = \frac{\tilde{\alpha}(k_{kin} + k_{diff,q})}{k_{kin} + \tilde{\alpha}k_{diff,q}}. \tag{62}$$

Solving for the Sherwood correction factor, $\tilde{\alpha}$, yields:

$$\tilde{\alpha} = \frac{\beta k_{kin}}{k_{kin} + k_{diff,q}(1-\beta)}. \tag{63}$$

This expression takes into account the effect of the ratio between the kinetic and the diffusive rate on the Sherwood correction factor. When $k_{kin} \gg k_{diff}$, $\tilde{\alpha}$ is nearly proportional to β. However, when the reaction is kinetically controlled, $\tilde{\alpha}$ is less dependent on β. In short, a Sherwood correction factor of 1 describes no change in the reaction rates in comparison to the homogeneous assumption *in a quiescent fluid*, a ratio $\tilde{\alpha} > 1$ signifies a speed-up, and a value $\tilde{\alpha} < 1$ corresponds to a slow-down.

In Section 6, the value of $d\overline{m}_p/dt$ is given by the actual mass loss rate obtained from the DNS simulation, while $d\overline{m}_{p,hom}/dt$ is found from Eq. (58). The Sherwood correction factor is then determined from Eq. (63).

5. Simulation setup

For simplicity, char is here considered to react with oxygen to form carbon dioxide. Hence, no homogeneous reactions are present, and the gas phase source term, $\dot{\omega}_k$ in Eq. (6), is zero. The heterogeneous mechanism is taken from the work of Li and You [58] and summarized in Table 1.

To achieve relatively constant Stokes and **Da** for the duration of the simulation, the particles react with oxygen present in the fluid

Table 1
Heterogeneous mechanism.

$C + O_2 \rightarrow CO_2$		
B_n[m/s]	α_n[−]	E_n[J/mol]
$1.2 \cdot 10^4$	0	$101 \cdot 10^3$

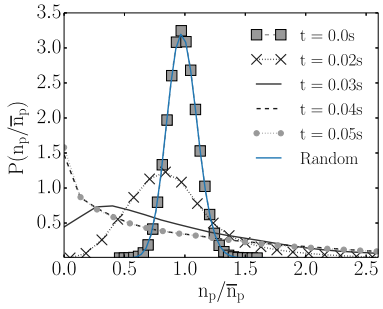

Fig. 1. Evolution of the PDF of the particle number density over time.

and transfer mass to the fluid phase while the particles themselves do not lose mass. It is done by adding the mass released by the particle to the fluid, but not substracting the released mass from the particle mass. This allows us to exclude the effects of varying Damköhler and Stokes numbers, and therefore different clustering or mass transfer behaviour, from the present analysis. The reactions assume a fully dried and devolatilized char particle reacting with oxygen in isotropic and homogeneous turbulence. This setup is meant to resemble what would be observed when studying a small fluid volume that is advected with the mean flow downstream of the zone of gas phase combustion. The Damköhler number is varied from simulation to simulation by varying the number of particles in the domain according to Eq. (48). For the present work, stoichiometric conditions are given for a Damköhler number of 0.1, which has 100k particles in the domain. To convert all oxygen in the domain to carbon dioxide, the carbon content of 100k particles with the employed density and radius is needed. In simulations with lower particle numbers than 100k, more mass is added to the fluid than is contained within the particles. As an example, when all oxygen of the simulation containing 50k particles has been converted to carbon dioxide, the particles have transferred two times their carbon content to the fluid. However, these simulations are well in the low Damköhler regime, and this stays unchanged from the beginning of the reactions to the time of full oxygen conversion, so results for the low Damköhler simulations are unaffected by this.

The use of periodic boundary conditions together with the ideal gas law results in a linear increase of pressure as the temperature in the domain increases. However, as the heterogeneous reaction is unimolar, the gas concentration is not affected. For the cases with the highest increase in temperature, the pressure rises to 1.5 times its initial value, but the reaction rates are unaffected by this except for the influence of the gas temperature on the diffusivity. The higher diffusivity increases the mass transfer rate to the particle surface, speeding up the reaction rates and counteracting the drop in reaction rates due to the decrease in oxygen content.

5.1. Initialization and start time of reactions

All cases are initialized with random particle positions and then run with reactions disabled until a statistically steady state is reached, which is determined by a stabilization of the shape of the PDF of the particle number density. The evolution of the PDF of the particle number density over time is presented in Fig. 1. The PDF for each time is evaluated by projecting the particle position

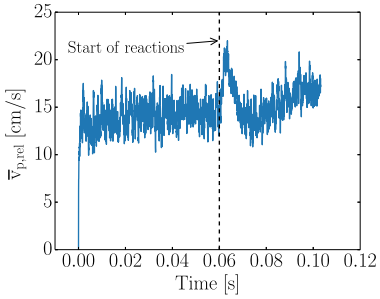

Fig. 2. Evolution of the relative particle velocity over time.

on the nearest node and smoothing the resulting scalar field with a clipped Gaussian filter of a width of seven nodes. The resulting values of the smoothed scalar field are then evaluated using 30 bins of equal width over the range of values. As can be seen, the initial distribution is close to a Gaussian distribution, which is expected from a true random distribution. As the simulationprogresses, the PDF broadens to show a high number of cells with few particles, but also a significant number of cells with many particles. This corresponds to clusters of particles, separated by voids with nearly no particles present. The mean relative velocity between the particles and the fluid varies around a constant value, as shown in Fig. 2 for a representative case. A simulation time of 0.06 s, which corresponds to 16 eddy turnover times, is sufficient to reach a statistically steady state for all cases. The long term variation in relative particle velocity that occur after the reactions are turned on is due to the effect of chemical reactions on temperature and fluid composition. Only data from when the mean oxygen mass faction is still above 1% is taken into account in the subsequent analysis.

5.2. Particle size to grid size dependence

Attention must be given to the fact that the ratio of the particle diameter to the square of the cell size should not exceed a certain value. If a single particle in a cell represents too much reactive surface, the cell's oxygen content is rapidly consumed and a region devoid of oxygen forms around the particle. In the work of Annamalai and Ramalingam [36], this zone is called the film zone and the particle is undergoing Individual Particle Combustion. This is a physical effect, which leads to a reaction rate that is lower than the ideal homogeneous reaction rate, even for small Damköhler numbers. In addition, particles that are large compared to the grid cell tend to introduce numerical instability in the simulations, and, in extreme cases, they will also violate the point-particle assumption that the particle tracking model is based upon. To mitigate these numerical issues, and the forming of a significant "film zone" around each particle, sufficiently small particles are needed. To hold the Damköhler number constant when decreasing the particle surface area, the number density n_p of particles has to be increased according to Eq. (44). This effect is illustrated in Fig. 3, where the Sherwood correction factor is shown to decrease for increasing oxygen conversion and larger ratios of $r_p/\Delta x^2$. The oxygen conversion is defined as:

$$c(t) = 1 - \frac{\overline{Y}_{O_2}(t)}{Y_{O_2,0}}. \tag{64}$$

Figure 4 shows the oxygen mass fraction for simulations with decreasing particle sizes and increasing particle numbers from left to right. All cases have the same low Damköhler number, and a domain size of 6.28 cm.

The areas of low oxygen content around single, large particles are particularly visible in the leftmost panel. Moving towards the right panel it is clear that for smaller particles, the oxygen

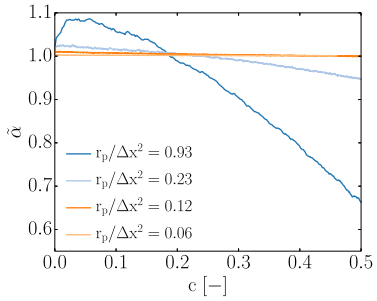

Fig. 3. Ratio of the real to the ideal homogeneous reaction rate for a constant Damköhler number of 0.1 for different particle sizes as a function of oxygen conversion.

Table 2
Common boundary conditions of the cases. Here, subscript 0 refers to the initial condition.

$T_{gas,\,0}$	2100 [K]
$T_{wall,\,0}$	2100 [K]
$T_{p,\,0}$	2100 [K]
ρ_{char}	8.55 [g/cm^3]
ρ_{gas}	$3{\cdot}10^{-4}$ [g/cm^3]
u_{RMS}	180.0 [cm/s]
Re	40 [-]
L_f	$2\pi/1.5$ [cm^{-1}]
$Y_{CO_2,0}$	0.74 [-]
$Y_{O_2,0}$	0.26 [-]
L_{dom}	6.28 [cm]
r_p	11.25 [µm]
N_{cell}	64^3 [-]

distribution is more uniform. When decreasing the particle size, the Damköhler number is kept constant by increasing the particle number density. For turbulent cases, it is also important to maintain the same Stokes number, which is achieved by increasing the material density of the particles.

The Sherwood correction factor is shown as a function of the particle size ($r_p/\Delta x^2$) for Da = 0.1 in Fig. 5. It can be seen from the figure that the Sherwood correction factor starts to decrease for $r_p/\Delta x^2 > 0.12$. This decrease is, as explained previously, due to the presence of a film zone with lower oxygen around the large particles. To avoid having to account for the effect of the film zone, a particle radius of 11.257 µm ($r_p/\Delta x^2 = 0.12$) is chosen for the remainder of the simulations. To satisfy the requirement of a Stokes number of unity and much smaller particle diameter than the grid size, a large density ratio between particle and fluid is required. This would not be a requirement for larger Reynolds numbers though, since the flow time scale would be reduced. The requirement for a high density ratio results in very dense, small particles, that move like char particles with a diameter of 50 µm and a density of 0.7 g/cm^3. Table 2 summarizes the general conditions of all simulations.

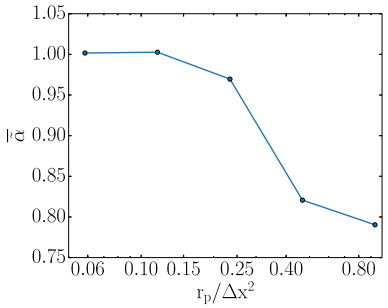

Fig. 5. Ratio of the real to the ideal homogeneous reaction rate for a constant Damköhler number of 0.1 over the ratio $r_p/\Delta x^2$.

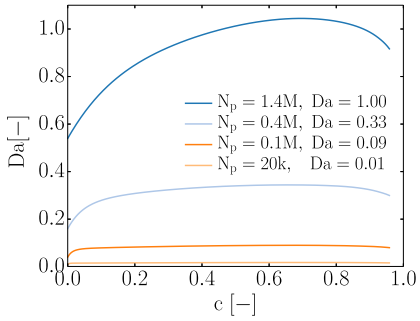

Fig. 6. Evolution of the Damköhler number over conversion.

6. Results

Figure 6 shows the Damköhler number as given by Eq. (45) as a function of oxygen conversion for cases with different particle number densities. Higher particle number densities yield higher Da, and the Damköhler number for each case increases until 75% conversion, and then decreases again. The change in fluid diffusivity with temperature is the most important fluid property influencing the variability of the Damköhler number.

Figure 7 shows the ratio of the kinetic to the mass transfer rate for cases with different Da, plotted as a function of oxygen conversion. The ratio first increases, with the maximum being higher for lower Da. The reason for this is that the amount of oxidizer per particle is higher for lower Da. This means that for low Da, the particles obtain higher temperatures, and hence larger values of k_{kin}. The decrease in the kinetic rate at later times is due to radiative particle cooling. It is clear from the figure that for these simulations, the char conversion is diffusion controlled for low Damköhler numbers.

6.1. The reaction rate, oxygen consumption and inhibition

The decrease of oxygen content over time can be seen in Fig. 8 for several Da. The x-axis is at 1% Y_{O_2}, which illustrates the large

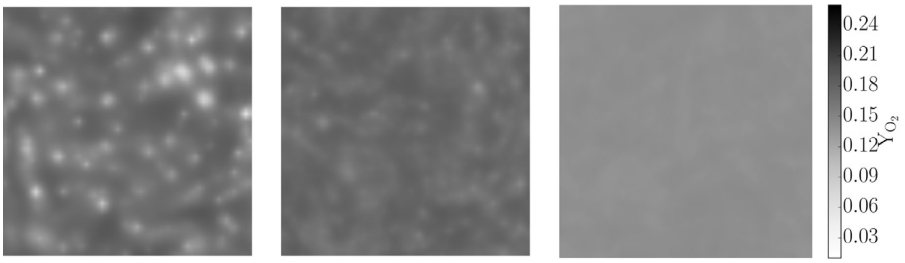

Fig. 4. Plots of the oxygen mass fraction for cases with increasing particle numbers and decreasing particle radii at a low and constant Damköhler number.

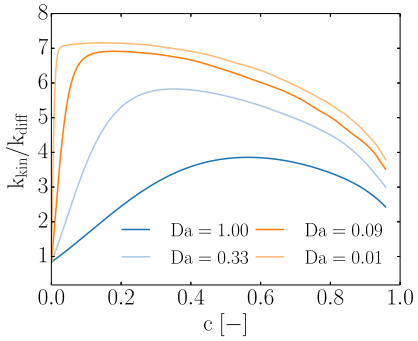

Fig. 7. Ratio of kinetic and mass transfer rate over conversion.

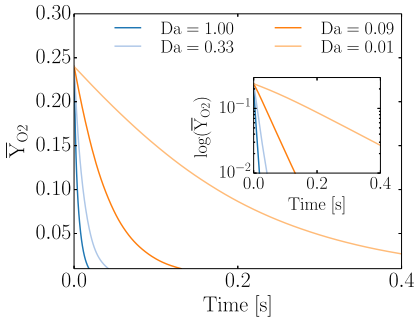

Fig. 8. Evolution of the mean oxygen mass fraction over time.

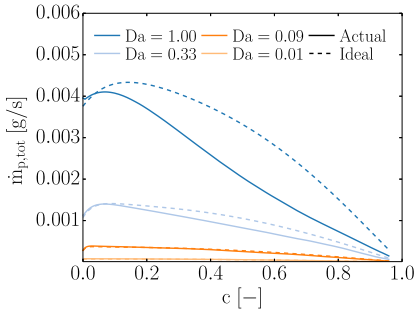

Fig. 9. Comparison of ideal and actual total particle mass loss rates over conversion for simulations with different Da.

differences in time to reach this mass fraction. The case with the highest Damköhler number reaches 1% mass fraction of oxygen after 0.02 s, while the case with the lowest Damköhler number takes 60 times longer, i.e. 1.2 s. The mean oxygen mass fraction decreases near exponentially, which can be seen in the inset. The exponential decay is expected from a first order reaction equation [43].

In Fig. 9, the actual total particle mass loss rate ($d\overline{m}_p/dt$) and the ideal homogeneous mass loss rate ($d\overline{m}_{p,hom}/dt$), assuming homogeneous distribution of particles, are compared for several Da. For low conversions (early times), all cases show comparable ideal and actual mass loss rates. For higher conversion values, the ideal mass loss is higher than the actual one, and the difference is stronger for higher **Da**.

The fastest reactions are found in the beginning, when oxygen is still available inside the particle clusters. The reason for the difference between the ideal and the actual mass loss for high **Da** is that the particle clusters become void of oxygen, even though there are large amounts of oxygen available between the clusters. This means that the ideal homogeneous mass loss is only taking into account the total amount of oxygen in the domain or cell, while the actual mass loss is also taking into account the distribution of oxygen and particles. Figure 10 shows the corresponding Sherwood correction factor over conversion, as obtained from Eq. (63), for the same cases as was shown in Fig. 9. The curve ends when the mass fraction of oxygen has reached 1%. The decrease of the Sherwood correction factor for high **Da** is clearly seen. It can also be seen that the Sherwood correction factor has a tendency to decrease with conversion for conversions less than about 50%. The reason that the Sherwood correction factor is higher for early times is that the particles clusters are not yet void of oxygen. For larger conversions, a clear positive or negative trend in the behaviour of the Sherwood correction factor is no longer seen, and we therefore choose to define the steady state Sherwood correction factor as the value obtained in the range from 50%–99% conversion.

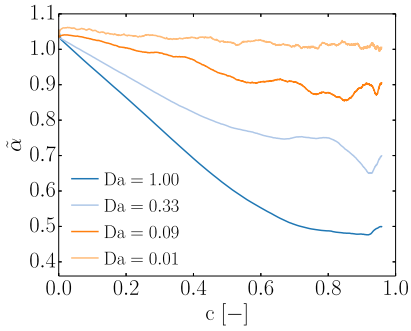

Fig. 10. Sherwood correction factor over conversion for simulations with different Damköhler numbers.

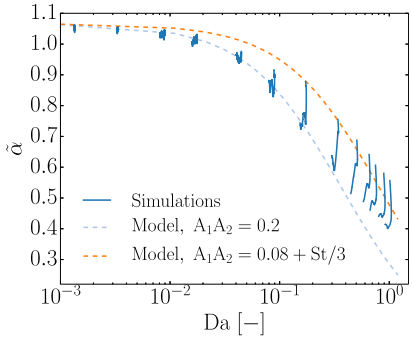

Fig. 11. Sherwood correction factor over the Damköhler number.

In Fig. 11, the steady state Sherwood correction factor is plotted over Damköhler number for a range of different simulations. The small scale influence of turbulence can be seen in the fact that for small Da, the reaction rate is faster than the ideal homogeneous one (i.e. $\tilde{\alpha} > 1$). This is due to the fact that the turbulence induces a relative velocity between the particles and the fluid, which results in fresh reactants constantly being convected to the particle surface, and hence, that the conversion rate is increased.

For large Damköhler numbers ($\mathrm{Da} > 0.3$), the Sherwood correction factor is less than unity. This is due to the effect of the particle clustering, where the fluid in the particle clusters are depleted of oxygen, while there is still significant amounts of oxygen left in the volumes between the clusters. The dashed lines in Fig. 11 represent the model for the Sherwood correction factor, as given by Eq. (54), where the cluster dependent reaction rate, α_{cl}, is given by Eq. (51). The Sherwood number can be found from Eq. (39), when utilizing the model for the relative particle-fluid velocity that was developed by Haugen et al. [44]. Furthermore, for the upper orange dashed line, the value of A_1A_2 used in Eq. (51) is given by $A_1A_2 = 0.08 + \mathrm{St}/3$, which is taken from Haugen et al. [44]. For comparison, the light blue lower dashed line has been obtained by using $A_1A_2 = 0.2$. It can be seen that the qualitative behaviour of Eq. (54) is fairly similar to the results from the DNS. The model

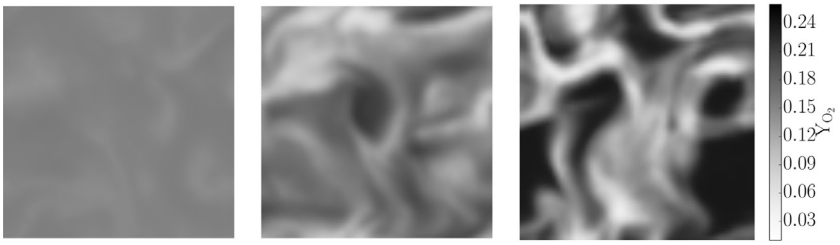

Fig. 12. Plots of the oxygen mass fraction for cases with increasing Da, 0.01, 0.09 and 1.00 from left to right, $\bar{Y}_{O_2} = 15\%$, the time of the snapshots is 100ms, 6ms and 2ms from left to right.

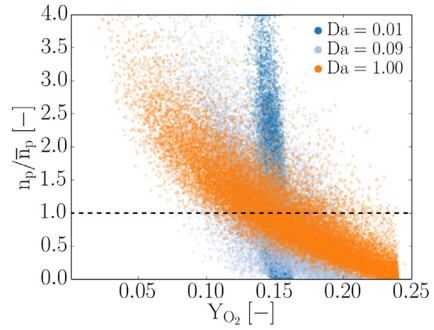

Fig. 13. Scatter plot of the particle number density over the oxygen mass fraction. The mean oxygen mass fraction is $\overline{Y}_{O_2} = 15\%$ for all three simulations.

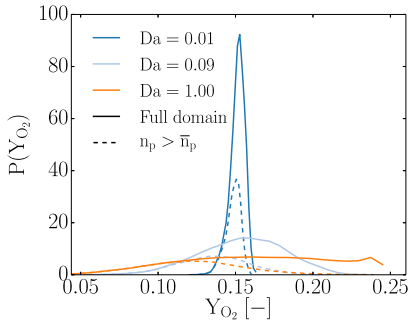

Fig. 14. PDF of the oxygen mass fraction for the full domain (continuous lines) and in regions where $n_p > \bar{n}_p$ (dashed lines). Higher **Da** result in broader distributions.

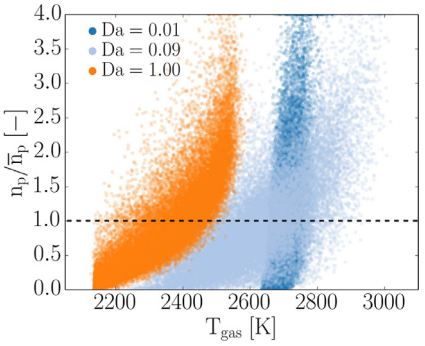

Fig. 15. Scatter plot of the particle number over the domain temperature.

for A_1A_2 as found by Haugen et al. [44], yields a surprisingly good result, even though the physics in their case was more simplified and only mass transfer was considered. This supports the assumption that it is primarily the mass transfer effect that is influenced by the turbulence. We do believe though, that the discrepancy between the simulation results and the model results (orange upper dashed line) is due to the interaction between turbulence and heat transfer that is not taken into account by the model. The heat transfer is expected to be influenced by the turbulence in a similar way as is the case for mass transfer. This effect would be divided into a Nusselt number influence due to slip velocity between particle and fluid, and due to particle clustering, decreasing the overall heat transfer rate. Finally, it could also be noted that a higher Damköhler number yields a higher variance in the Sherwood correction factor, while the variance is fairly small for the smaller Da.

6.2. The distribution of oxygen and temperature in the domain

Figure 12 shows the instantaneous value of the oxygen mass fraction in a slice of the domain when the mean oxygen mass fraction is 15% for three cases with increasing **Da** from left to right. A distinct increase in the difference between the oxygen rich and lean regions is clearly visible for higher Da.

A high Damköhler number results in a large variance in the oxygen mass fraction, as clusters become depleted of oxygen in a short time, while the regions with low particle number density are left nearly untouched. This effect can be observed in Fig. 13, where a scatter plot of the normalized particle number density as a function of the oxygen mass fraction is shown. The low Damköhler case shows very similar levels of oxygen content for all particle number densities, while the large Damköhler case shows a clear correlation between high relative particle number densities and low oxygen content. In Fig. 14 the corresponding PDF of the oxygen mass fraction is shown. The constrained probabilities for regions where the particle number density is higher than its mean value, $n_p > \overline{n}_p$ (dashed line in Fig. 13), have different positions in the overall distribution. While the constrained distribution for low **Da** fills nearly the full range of values of the unconstrained one, the constrained distribution for the large Damköhler case only covers the lower half of the unconstrained range of values. The values of oxygen mass fraction have a larger spread for higher Da. Note that the mean oxygen mass fraction for all cases at the time of the snapshot was around 15%, hence the data is from different times (see Fig. 8).

Finally the effect of turbulence on the temperature distribution in the domain is studied. The normalized particle number density is plotted as a function of the gas temperature in Fig. 15, and the resulting PDF of the gas temperature is shown in Fig. 16. The mean oxygen mass fraction is 15% for all cases. A higher Damköhler number simulation has a wider range of temperatures and a lower mean temperature than simulations of lower Da. The lower mean temperature of the high Damköhler cases is explained by the high number of particles in the domain, which constitute a higher fraction of the energy stored in the particles, and an increase in radiation losses from the sum of all particles. This is due to the particles' radiative heat loss being the only heat sink in the system, which is proportional to the number of particles in the domain. It can also be seen that the gas in particle clusters tends to be hotter than the one with a lower particle density. The wide range of temperatures found for medium **Da** is believed to be due to the wide

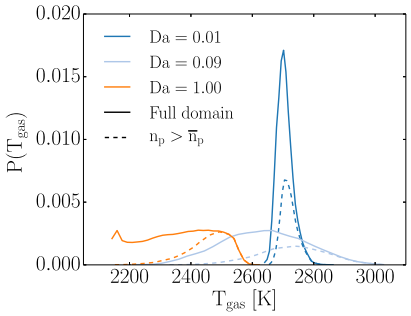

Fig. 16. PDF of the domain temperature for cases with three different Da. The dashed line represents the subset of the domain where $n_p > \overline{n}_p$.

range of states the gas can be in. For medium Da, parts of the domain have already been emptied of oxygen and cooled down, while other parts have not yet been in contact with particles.

7. Conclusions

The simple model of Haugen et al. [44] and Krüger et al. [43], where DNS was used to analyse heterogeneous reactions in isotropic turbulence, has been extended to incorporate real species and temperature effects. It has been found that the particles form clusters because of the turbulence. Treating the reactions for high **Da** as only occurring on the outer shell of these particle clusters is found to give reasonable results, and a cluster dependent reaction rate α_{cl} is found to yield a good approximation of the maximum rate of reaction that can be achieved for heterogeneous reactions. Haugen et al. [44] has given an approximate value of A_1A_2, which fits the results reasonably well. The fitting factors A_1 and A_2 are factors relating to the number density and surface-to-volume ratio of the particle clusters, both of which depend on the shape of the clusters. Predicting the shape of the particle clusters, and thus values of A_1 and A_2 from flow field and particle properties is the topic of ongoing work. The simulations show the same trend as obtained in the work of Haugen et al. [44] and Krüger et al. [43]. However, using $A_1A_2 = 0.08 + \mathrm{St}/3$ slightly overpredicts the reaction rate for low and medium Da. For low and intermediate Da, a good fit is achieved with $A_1A_2 = 0.2$, at the cost of underprediction for higher Da. The developed model, as presented in Eq. (54), should be used in RANS simulations to account for the effect of turbulence on the conversion of heterogeneously reacting particles. The model accounts both for (1) the effect of increased mass transfer due to turbulence-induced relative velocities between particles and fluid, and (2) the effect of particle clustering.

The Sherwood correction factor, as given by Eq. (54) can be evaluated for e.g. each cell of a coarsely resolved simulation using known flow and particle variables. The mean Sherwood number $\overline{\mathrm{Sh}}$ can be approximated using a correlation for the relative velocity between particles and fluid, as described by Haugen et al. [44], and the cluster dependent reaction rate α_{cl} can be found from Eq. (51). The Sherwood correction factor can then be inserted into Eq. (55) to yield a turbulent mass transfer coefficient that accounts for the effect of turbulence;

$$k_{diff,turb} = \frac{D\tilde{\alpha}}{r_p}. \tag{65}$$

Applying this modified mass transfer coefficient to each particle in one computational cell accounts for the unresolved clustering and slip velocities of particles. The reason for the discrepancies between the results obtained in this work and the results of Haugen et al. [44] are thought to be due to the thermal and kinetic effects that have been included in the current work. In the work of Haugen et al. [44], the consumption of a passive scalar is studied, which does not influence the carrier fluid. Meanwhile, the consumption of oxygen directly affects the density, temperature, composition and momentum of the fluid. Another difference is the lower flow Reynolds number of approximately 40 that has been studied here, while the work of Haugen et al. studies flows with Reynolds numbers in the range of 80–2200.

The Sherwood correction factor is also dependent on the size ratio of the particles and the grid cells size, which are all factors that influence the cost of the simulations. The ratio of particle to grid cell size in the present work was chosen so that the reaction rates at small **Da** behave similar to the homogeneous assumption at reasonable cost and ensure the validity of the point-particle assumption. Increasing the particle size will yield lower Sherwood correction factors. In addition, it tends to yield numerical instabilities.

It is worth noting that extending this analysis to include several heterogeneous and homogeneous reactions will complicate the interpretation of the effect of turbulence. Interestingly, this can result in cases where production/consumption of one species can be modelled by the homogeneous approach, while other species' reactions are happening at the cluster dependent reaction rate.

The proposed model gives a good approximation of the char consumption rate in reacting flows with heterogeneous reactions. Note that the current work deals with devolatilized char particles. It has been found that, although both devolatilization and heterogeneous combustion feature a wide range of time scales [59], devolatilization and homogeneous combustion of the devolatilized fuel are up to a magnitude faster than char conversion [30]. Depending on the gas temperature and particle diameter, a diffusion flame exists around a devolatilizing particle, preventing oxygen from reaching the particle until the fuel particle is fully devolatilized [60]. This results in two distinct reaction regimes, coal devolatilization and char combustion, where char combustion is proceeding at a much slower rate [61]. To further improve its predictability, more work has to be done to identify an appropriate correlation for A_1A_2, and to analyse the effect of several heterogeneous and homogeneous reactions, especially for cases where non-unimolar reactions are considered. The effects of particle heating and heat transfer between fluid and particles should also be examined. Another important unknown effect is the influence of the particle diameter. Simulations with particles with a range of sizes have to be performed, as their different clustering behaviour will yield different, probably less extreme effects compared with the present work.

Acknowledgments

The research leading to these results has received funding from the Polish-Norwegian Research Programme operated by the National Centre for Research and Development under the Norwegian Financial Mechanism 2009–2014 in the frame of Project Contract No Pol-Nor/232738/101/2014.

References

[1] N. Hashimoto, R. Kurose, H. Shirai, Numerical simulation of pulverized coal jet flame employing the TDP model, Fuel 97 (2012) 277–287.
[2] N. Hashimoto, H. Watanabe, Numerical analysis on effect of furnace scale on heat transfer mechanism of coal particles in pulverized coal combustion field, Fuel Processing Technology 145 (2016) 20–30, doi:10.1016/j.fuproc.2016.01.024.
[3] Ansys Inc., Ansys 15.0 theory guide (2014). Available at http://www.ansys.com/
[4] J.-P. Minier, E. Peirano, The pdf approach to turbulent polydispersed two-phase flows, Phys. Rep. 352 (13) (2001) 1–214, doi:10.1016/S0370-1573(01)00011-4.
[5] M. Stöllinger, B. Naud, D. Roekaerts, N. Beishuizen, S. Heinz, PDF modeling and simulations of pulverized coal combustion Part 1: Theory and modeling, Combust. Flame 160 (2) (2013) 384–395, doi:10.1016/j.combustflame.2012.10.010.
[6] M. Stöllinger, B. Naud, D. Roekaerts, N. Beishuizen, S. Heinz, PDF modeling and simulations of pulverized coal combustion part 2: Application, Combust. Flame 160 (2) (2013b) 396–410, doi:10.1016/j.combustflame.2012.10.011.

[7] G. Olenik, O. Stein, A. Kronenburg, LES of swirl-stabilised pulverised coal combustion in IFRF furnace no. 1, Proc. Combust. Inst. 35 (3) (2015) 2819–2828, doi:10.1016/j.proci.2014.06.149.

[8] O.T. Stein, G. Olenik, A. Kronenburg, F. Cavallo Marincola, B.M. Franchetti, A.M. Kempf, M. Ghiani, M. Vascellari, C. Hasse, Towards comprehensive coal combustion modelling for LES, Flow, Turbul. Combust. 90 (4) (2013) 859–884, doi:10.1007/s10494-012-9423-y.

[9] J. Watanabe, T. Okazaki, K. Yamamoto, K. Kuramashi, A. Baba, Large-eddy simulation of pulverized coal combustion using flamelet model, Proc. Combust. Inst. (2016), doi:10.1016/j.proci.2016.06.031.

[10] M.M. Baum, P.J. Street, Predicting the combustion behaviour of coal particles, Combust. Sci. Technol. 3 (5) (1971) 231–243, doi:10.1080/00102207108952290.

[11] I. Smith, The intrinsic reactivity of carbon to oxygen, Fuel 57 (1978) 409–414.

[12] J. Watanabe, T. Okazaki, K. Yamamoto, K. Kuramashi, A. Baba, Large-Eddy simulation of pulverized coal combustion using flamelet model, Proc. Combust. Inst. 36 (2) (2017) 2155–2163, doi:10.1016/j.proci.2016.06.031.

[13] J.H. Chen, A. Choudhary, B. de Supinski, M. DeVries, E.R. Hawkes, S. Klasky, W.K. Liao, K.L. Ma, J. Mellor-Crummey, N. Podhorszki, R. Sankaran, S. Shende, C.S. Yoo, Terascale direct numerical simulations of turbulent combustion using s3d, Comput. Sci. Disc. 2 (1) (2009) 015001.

[14] J. Kim, P. Moin, R. Moser, Turbulence statistics in fully developed channel flow at low reynolds number, J. Fluid Mech 177 (1987) 133–166.

[15] D. Spalding, Mixing and chemical reaction in steady confined turbulent flames, Symp. (Int.) Combust. (1971) 649–657.

[16] S.B. Pope, Pdf method for turbulent reacting flows., Progr. Energy Combust. Sci. 11 (1985) 119–195.

[17] K. Bray, J. Moss, A unified statistical model of the premixed turbulent flame, Acta Astronautica 4 (3) (1977) 291–319, doi:10.1016/0094-5765(77)90053-4.

[18] S. Pope, The evolution of surfaces in turbulence, Int. J. Eng. Sci. 26 (5) (1988) 445–469, doi:10.1016/0020-7225(88)90004-3.

[19] A.R. Kerstein, W.T. Ashurst, F.A. Williams, Field equation for interface propagation in an unsteady homogeneous flow field, Phys. Rev. A 37 (1988) 2728–2731, doi:10.1103/PhysRevA.37.2728.

[20] S. Burke, T. Schumann, Diffusion flames, Ind. Eng. Chem. 20 (1928) 998–1004.

[21] B. Magnussen, B. Hjertager, On mathematical models of turbulent combustion with special emphasis on soot formation and combustion, Symp. (Int.) Combust. 16 (1) (1979) 719729.

[22] A.Y. Klimenko, Multicomponent diffusion of various admixtures in turbulent flow, Fluid Dyn. 25 (3) (1990) 327–334, doi:10.1007/BF01049811.

[23] R.W. Bilger, Conditional moment closure for turbulent reacting flows, Phys. Fluids A Fluid Dyn. 5 (2) (1993) 436–444, doi:10.1063/1.858867.

[24] H. Pitsch, M. Ihme, An unsteady/flamelet progress variable method for LES of nonpremixed turbulent combustion, Aerospace Sciences Meetings, American Institute of Aeronautics and Astronautics (2005), doi:10.2514/6.2005-557.

[25] N. Peters, Laminar flame concepts in turbulent combustion, Symp. (Int.) Combust. 21 (1986) 1231–1250.

[26] D. Veynante, L. Vervisch, Turbulent combustion modeling, Progr. Energy Combust. Sci. 28 (3) (2002) 193–266, doi:10.1016/S0360-1285(01)00017-X.

[27] T. Poinsot, D. Veynante, Theoretical and numerical combustion, 2012.

[28] M.L. de Souza-Santos (Ed.), Solid fuels combustion and gasification, CRC Press, 2010, doi:10.1201/9781420047509.

[29] K. Luo, H. Wang, J. Fan, F. Yi, Direct numerical simulation of pulverized coal combustion in a hot vitiated co-flow, Energy Fuels 26 (10) (2012) 6128–6136, doi:10.1021/ef301253y.

[30] A. Richter, P.A. Nikrityuk, M. Kestel, Numerical investigation of a chemically reacting carbon particle moving in a hot o2/co2 atmosphere, Ind. Eng. Chem. Res. 52 (16) (2013) 5815–5824, doi:10.1021/ie302770j.

[31] A. Eaton, L. Smoot, S. Hill, C. Eatough, Components, formulations, solutions, evaluation, and application of comprehensive combustion models, Progr. Energy Combust. Sci. 25 (4) (1999) 387–436, doi:10.1016/S0360-1285(99)00008-8.

[32] W.E. Ranz, W.R. Marshall, Evaporation from drops, Chem. Eng. Progr. 48 (1952) 141–146.

[33] J.K. Eaton, J.R. Fessler, Preferential concentration of particles by turbulence, Int. J. Multiph. Flow 20 (1994) 169–209.

[34] A.M. Wood, W. Hwang, J.K. Eaton, Preferential concentration of particles in homogeneous and isotropic turbulence, Int. J. Multiph. Flow 31 (2005) 1220–1230.

[35] J. Bec, Fractal clustering of inertial particles in random flows, Phys. Fluids 15 (11) (2003) L81–L84, doi:10.1063/1.1612500.

[36] K. Annamalai, S. Ramalingam, Group combustion of char carbon particles, Combust. Flame 70 (3) (1987) 307–332, doi:10.1016/0010-2180(87)90111-8.

[37] J. Reveillon, F. Demoulin, Evaporating droplets in turbulent reacting flows, Proc. Combust. Inst. 31 (2) (2007) 2319–2326, doi:10.1016/j.proci.2006.07.114.

[38] Y. Bai, K. Luo, K. Qiu, J. Fan, Numerical investigation of two-phase flame structures in a simplified coal jet flame, Fuel 182 (2016) 944–957, doi:10.1016/j.fuel.2016.05.086.

[39] T. Hara, M. Muto, T. Kitano, R. Kurose, S. Komori, Direct numerical simulation of a pulverized coal jet flame employing a global volatile matter reaction scheme based on detailed reaction mechanism, Combust. Flame 162 (12) (2015) 4391–4407, doi:10.1016/j.combustflame.2015.07.027.

[40] T. Brosh, N. Chakraborty, Effects of equivalence ratio and turbulent velocity fluctuation on early stages of pulverized coal combustion following localized ignition: A direct numerical simulation analysis, Energy Fuels 28 (2014) 6077-0688.

[41] T. Brosh, D. Patel, D. Wacks, N. Chakraborty, Numerical investigation of localised forced ignition of pulverised coal particle-laden mixtures: A direct numerical simulation (DNS) analysis, Fuel 145 (2015) 50–62.

[42] M. Muto, K. Yuasa, R. Kurose, Numerical simulation of ignition in pulverized coal combustion with detailed chemical reaction mechanism, Fuel 190 (2017) 136–144, doi:10.1016/j.fuel.2016.11.029.

[43] J. Krüger, N.E. Haugen, D. Mitra, T. Løvås, The effect of turbulent clustering on particle reactivity, Proc. Combust. Inst. (2016), doi:10.1016/j.proci.2016.06.187.

[44] N.E. Haugen, J. Krüger, D. Mitra, T. Løvås, The effect of turbulence on mass and heat transfer rates of small inertial particles, J. Fluid Mech (submitted), arxiv:1701.04567v1.

[45] M.B. Tilghman, R.E. Mitchell, Coal and biomass char reactivities in gasification and combustion environments, Combust. Flame 100 (2014) 100–101.

[46] M.B. Tilghman, N.E.L. Haugen, R.E. Mitchell, A comprehensive char-particle gasification model adequate for entrained-flow and fluidized-bed gasifiers, Energy Fuels (2017), doi:10.1021/acs.energyfuels.6b02148.

[47] L. Chen, S.Z. Yong, A.F. Ghoniem, Oxy-fuel combustion of pulverized coal: Characterization, fundamentals, stabilization and CFD modeling, Progr. Energy Combust. Sci. 38 (2) (2012) 156–214, doi:10.1016/j.pecs.2011.09.003.

[48] A. Brandenburg, Pencil code homepage (2014). Available at http://pencil-code.nordita.org/

[49] J. Williamson, Low-storage Runge-Kutta schemes, J. Comput. Phys. 35 (1) (1980) 48–56, doi:10.1016/0021-9991(80)90033-9.

[50] N. Babkovskaia, N. Haugen, A. Brandenburg, A high-order public domain code for direct numerical simulations of turbulent combustion, J. Comput. Phys. 230 (1) (2011) 1–12, doi:10.1016/j.jcp.2010.08.028.

[51] A. Brandenburg, N.E. Haugen, N. Babkovskaia, Turbulent front speed in the fisher equation: Dependence on Damköhler number, Phys. Rev. 83 (2011).

[52] N.E.L. Haugen, M.B. Tilghman, R.E. Mitchell, The conversion mode of a porous carbon particle during oxidation and gasification, Combust. Flame 161 (2) (2014) 612–619, doi:10.1016/j.combustflame.2013.09.012.

[53] S. Sundaram, L.R. Collins, Numerical considerations in simulating a turbulent suspension of finite-volume particles, J. Comput. Phys. 124 (2) (1996) 337–350, doi:10.1006/jcph.1996.0064.

[54] K.D. Squires, J.K. Eaton, Particle response and turbulence modification in isotropic turbulence, Phys. Fluids 7 (1990) 1191–12–3.

[55] S. Elghobashi, G.C. Truesdell, On the two-way interaction between homogeneous turbulence and dispersed solid particles. I: Turbulence modification., Phys. Fluids A 5 (1993) 1790–1801.

[56] N.E.L. Haugen, R.E. Mitchell, M.B. Tilghman, A comprehensive model for char particle conversion in environments containing O2 and CO2, Combust. Flame 162 (4) (2015) 1455–1463, doi:10.1016/j.combustflame.2014.11.015.

[57] C.T. Crowe, J.D. Schwarzkopf, M. Sommerfeld, Y. Tsuji, Multiphase flows droplets, CRC Press, 2012.

[58] K. Li, C. You, Particle combustion model simultaneously considering a volatile and carbon reaction, Energy Fuels 24 (2010) 4178–4184.

[59] I. Smith, The combustion rates of coal chars: A review, Symp. (Int.) Combust. 19 (1) (1982) 1045–1065, doi:10.1016/S0082-0784(82)80281-6. Nineteenth Symposium (International) on Combustion

[60] C.R. Shaddix, A. Molina, Particle imaging of ignition and devolatilization of pulverized coal during oxy-fuel combustion, Proc. Combust. Inst. 32 (2) (2009) 2091–2098, doi:10.1016/j.proci.2008.06.157.

[61] J.J. Murphy, C.R. Shaddix, Combustion kinetics of coal chars in oxygen-enriched environments, Combust. Flame 144 (4) (2006) 710–729, doi:10.1016/j.combustflame.2005.08.039.